J. Fluid Mech. (2022), *vol*. 944, A17, doi:10.1017/jfm.2022.480

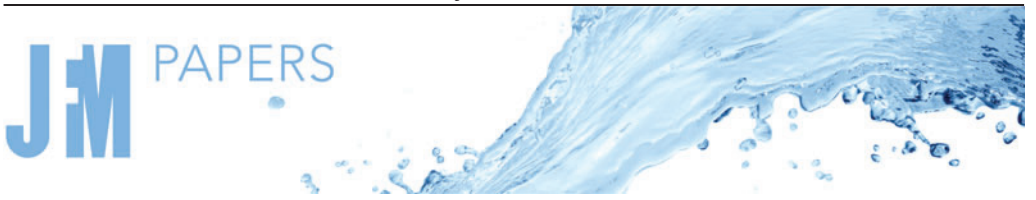

Microscopic pumping of viscous liquids with single cavitation bubbles

Hendrik Reese[1],†, **Robin Schädel**[1], **Fabian Reuter**[1] **and Claus-Dieter Ohl**[1]

[1]Department of Soft Matter, Institute of Physics, Otto-von-Guericke-University Magdeburg, Universitätsplatz 2, 39106 Magdeburg, Germany

(Received 22 December 2021; revised 18 March 2022; accepted 18 May 2022)

A cavitation bubble expanding and collapsing near a rigid boundary develops a directed jet flow towards the boundary. In the case of a perforated plate, some of the jet flow passes through the plate and thus the bubble acts as a pump transporting liquid from one side of the plate to the opposite side. The transport is rather complex, is time dependent and varies with the geometric parameters of the bubble and the connecting channel. Therefore, we first model the transport of liquid through a perforated rigid plate for a large range of parameters and then compare some regimes with experiments using single laser-induced bubbles. The simulations are based on a Volume-of-Fluid solver in OpenFOAM and account for surface tension, compressibility and viscosity. The resulting flux and generated velocity in the channel obtained in the simulations are discussed with regards to the dependence of the channel geometry, liquid viscosity and stand-off distance of the bubble to the plate. In general, high flow rates are achieved for long cylindrical channels that have a similar width as the jet produced by the collapsing bubble. At low stand-off distances combined with thick plates, an annular inflow creates a fast and thin jet, also called *needle jet*, which is approximately a magnitude faster and significantly thinner than the usually encountered microjet. In contrast, for thin plates and small stand-off distances, liquid is pumped in the opposite direction via a *reverse jet*.

Key words: bubble dynamics, cavitation, jets

1. Introduction

After Silberrad (1912) reported propeller erosion on the ships 'Lusitania' and 'Mauretania', Rayleigh (1917) proposed cavitation as the likely cause for the damage. The model named after him describes a collapsing spherical, empty cavity. He found that such a collapse creates high pressures in the liquid that may be responsible for the

† Email address for correspondence: hendrik.reese@ovgu.de

damage observed on the steel propellers. Improved spherical bubble models for example by Hickling & Plesset (1963) and later on Keller & Miksis (1980) include the pressure of non-condensable gas inside the bubble, liquid viscosity, surface tension and the energy loss from acoustic radiation. Boundaries that violate the spherical symmetry of the flow are not accounted for in these models. Early experimental investigations to understand the origin of erosion studied the effect of boundaries and geometries that break the spherical symmetry. For example, Shutler & Mesler (1965) studied the dynamics and collapse of a non-spherical spark-generated bubble near rigid plates, Benjamin & Ellis (1966) used an evacuated free fall device, and Lauterborn & Bolle (1975) introduced laser-induced cavitation bubbles to increase control on location and timing of the bubble. They all observed directed liquid flows or jets that form during the shrinkage of the bubble. Blake & Gibson (1987) developed a boundary element method to simulate the inviscid flow which helped to understand the mechanism of jet creation and the movement of the bubble towards the rigid boundary. Very good agreement between the experimental and the simulated bubble dynamics was found, see also Best & Kucera (1992).

As we know that an infinitely extended rigid boundary induces a jet towards the boundary, one may expect that a narrow diameter through-hole embedded in the boundary may not much alter the jetting dynamics. As a result, some of the liquid volume of the jet may be accelerated through the perforated boundary. This cavitation based liquid pump was first suggested by Khoo, Klaseboer & Hung (2005) in a numerical work using the boundary integral method to simulate a bubble near a plate with a small diameter through-hole. This was followed by experiments from Lew, Klaseboer & Khoo (2007) and later Karri *et al.* (2012*b*), who used a spark-generated bubble with a radius of several millimetres demonstrating the pumping mechanism. Dijkink & Ohl (2008) down-scaled the technique for microfluidic application using considerably smaller, laser-generated bubbles.

Karri *et al.* (2011) revealed that in the presence of a gaseous domain on the opposite side of the perforated plate, the bubble dynamics results in high-speed liquid jetting into the gas. The jet fragments into a spray of many smaller droplets. Initially, they used a lithotripter to create a bubble with $R_{max} \approx 250\,\mu$m, and later a spark discharge for a bubble with $R_{max} \approx 6$ mm (see Karri *et al.* 2012*a*). Further investigations of such jets and sprays were performed by Gonzalez-Avila, Song & Ohl (2015) and Kannan, Balusamy & Karri (2015) using a spark-generated bubble very close to a plate with a hole, with $R_{max} = 1$ and 8 mm, respectively.

Wang *et al.* (2013) experimentally studied the dynamics of a spark-generated cavitation bubble with length scales of millimetres near a thin perforated plate. Numerical investigations were performed by Dawoodian, Dadvand & Nematollahi (2015) using the boundary element method to simulate a bubble in a tube near a thin plate with a hole. Continuous pumping of the liquid has been demonstrated by Cao, Liu & Qu (2017) with periodically created cavitation bubbles just above a channel of radius $r_c = 2.5\,\mu$m. The particular shape of the plate has an effect on the bubble and therefore on the pumping as demonstrated by Cui *et al.* (2013), who conducted cavitation experiments with relatively large bubbles on top of a curved perforated plate. The experiments were later simulated by Moloudi *et al.* (2019) based on the boundary element method and, for certain parameters, revealed a pronounced jet in the opposite direction. However, the simulations stopped once the jet pierced the bubble and the resulting fluid transport past that instant was not obtained.

While there is strong experimental support for the pumping effect of bubbles near through-holes, there is a considerable lack in numerical simulations that include the jetting dynamics through the hole and the following bubble dynamics, and that study the influence

of various geometrical parameters of the hole as well as viscosity. These aspects are addressed in the present work, which also accounts for surface tension and compressibility of the liquid and the gas.

We start with a description of the governing flow equations and continue with the implementation in a Volume-of-Fluid (VoF) solver in § 3. Selected simulation results are compared to experiments. Therefore, we describe a suitable experimental setup in § 4 that can reveal not only the bubble dynamics but also the liquid transport. The results section starts with a detailed description of the pumping mechanism (§ 5.1). Then, the influence of various parameters on the pumping effectiveness are revealed and discussed in § 5.2. We then take a closer look at two particular flow phenomena in § 6, namely the so-called *needle jet* and the *reverse jet* using and comparing simulations with experiments, before we discuss and summarise the results.

2. Governing equations

The simulation model describes two immiscible, compressible, viscous fluids, i.e. water and a non-condensable gas, and accounts for their surface tension. Mass and heat transfer across the fluid–fluid interface are neglected. The initial process of cavitation nucleation, e.g. from a laser or a spark discharge, is ignored. Instead we start the fluid mechanics model with a small gas bubble at a high pressure at time $t = 0$.

The fluids satisfy the continuity equation (2.1) and the law of conservation of momentum (2.2) of Newtonian fluids,

$$\frac{\partial \rho}{\partial t} + \nabla \cdot (\rho \boldsymbol{u}) = 0, \tag{2.1}$$

$$\rho \frac{\mathrm{D}\boldsymbol{u}}{\mathrm{D}t} = \rho \boldsymbol{f} - \nabla p + \mu \left(\Delta \boldsymbol{u} + \frac{1}{3} \nabla (\nabla \cdot \boldsymbol{u}) \right). \tag{2.2}$$

Here, the physical quantities are density ρ, time t, velocity $\boldsymbol{u}$, volume acceleration $\boldsymbol{f}$ (e.g. gravity) and the dynamic viscosity μ. A liquid viscosity of $\mu = 1\,\mathrm{mPa\,s}$ and a gas viscosity of $\mu = 0.0184\,\mathrm{mPa\,s}$ are used, as well as a surface tension of $\sigma = 70\,\mathrm{mN\,m^{-1}}$. For both components, the Tait equation is used as an equation of state:

$$p = (p_0 + B) \left(\frac{\rho}{\rho_0} \right)^{\gamma} - B, \tag{2.3}$$

where the constants are $p_0 = 101\,325\,\mathrm{Pa}$, $B = 303.6\,\mathrm{MPa}$, $\rho_0 = 998.21\,\mathrm{kg\,m^{-3}}$, and $\gamma = 7.15$ for the liquid (water) and $p_0 = 10\,320\,\mathrm{Pa}$, $B = 0$, $\rho_0 = 1\,\mathrm{kg\,m^{-3}}$, and $\gamma = 1.33$ for the gas. With $B = 0$, the equation of state (2.3) describes the adiabatic change of state of an ideal gas.

The Rayleigh collapse time is the idealised time it takes for an empty cavity under the action of a constant external pressure to shrink to zero size. Lord Rayleigh solved the energy equation for an inviscid, incompressible fluid initially at rest once a portion of the liquid was instantaneously removed (see Rayleigh 1917). He obtained an equation for the bubble radius as a function of time that could be integrated to obtain the Rayleigh collapse time

$$\tau \approx 0.91468\, R_{max} \sqrt{\frac{\rho}{p_0}}. \tag{2.4}$$

This Rayleigh collapse time is approximately $\tau = 46\,\mu\mathrm{s}$ for typical bubbles of $R_{max} = 0.5\,\mathrm{mm}$. The spherical bubble dynamics obtained from the VoF solver can be compared to

the Keller–Miksis model (Keller & Miksis 1980):

$$R\ddot{R}\left(1-\frac{\dot{R}}{c}\right)+\frac{3}{2}\dot{R}^2\left(1-\frac{\dot{R}}{3c}\right)+\frac{4\nu\dot{R}}{R}+\frac{2\sigma}{\rho R}+\frac{p_0-p_g}{\rho}\left(1+\frac{\dot{R}}{c}\right)-\frac{R\dot{p}_g}{\rho c}=0, \quad (2.5)$$

which is a solution to the Navier–Stokes equation and accounts for compressibility in the limit of linear acoustic waves.

3. Numerical implementation

3.1. *Numerical solver*

For the simulations, a modified version of the VoF solver COMPRESSIBLEINTERFOAM from the open-source framework OpenFOAM 4.0 (2016) is used. It models two compressible, non-isothermal, immiscible fluids using a phase-fraction based interface capturing scheme. The solutions are obtained in 250 000 to 370 000 computational cells, each of which is assigned its respective flow equations. The solver solves for the five fields pressure p, non-gravitational pressure $p_{rgh} = p - \rho\, \boldsymbol{g}\cdot\boldsymbol{r}$, velocity $\boldsymbol{u}$, temperature T and phase fraction α, which is a non-dimensional scalar field ranging between 0 and 1 that specifies the relative volume amount of a cell occupied by one of the fluids. In this case, $\alpha = 1$ means that a cell is fully occupied by water and $\alpha = 0$ means it is fully occupied by gas. Since gravitational effects are neglected, $\boldsymbol{g}$ is chosen to be 0 and thus $p_{rgh} = p$.

The solver is derived from CAVBUBBLEFOAM by Koch *et al.* (2016) and Zeng *et al.* (2018), which itself was a modification of the original COMPRESSIBLEINTERFOAM. CAVBUBBLEFOAM updates the compressibility field in every time step and neglects non-isothermal effects by removing the temperature equation. This simplification has been used successfully for cavitation bubble simulations by Zeng *et al.* (2018).

In each time step, the equations for α, ρ, $\boldsymbol{u}$ and p are solved. In the following, the notation $\alpha_1 := \alpha, \alpha_2 := 1-\alpha$ is used. Since phase transitions are ignored, each component satisfies the continuity equation separately (2.1), i.e.

$$\frac{\partial(\alpha_j\rho_j)}{\partial t}+\nabla\cdot(\alpha_j\rho_j\boldsymbol{\phi})=0, \quad (3.1)$$

where $\boldsymbol{\phi}$ denotes the interpolation of $\boldsymbol{u}$ at the cell faces since $\boldsymbol{u}$ is only defined at the centre of each cell and $j = 1, 2$ represents the two fluid components. By using the definition of the compressibility, $\mathrm{d}\rho_j = \psi_j\,\mathrm{d}p$, (3.1) yields

$$\frac{\partial\alpha_1}{\partial t}+\nabla\cdot(\alpha_1\boldsymbol{\phi})+\frac{\alpha_1}{\rho_1}\psi_1\frac{Dp}{Dt}+\nabla\cdot(\alpha_1\alpha_2\boldsymbol{\phi}_r)=0. \quad (3.2)$$

The last term on the left-hand side was added to counteract the smearing of the fluid–fluid interface due to numerical diffusion. The vector $\boldsymbol{\phi}_r$ is defined as

$$\boldsymbol{\phi}_r = c_\alpha\sum_i\frac{|\phi_i|}{|\boldsymbol{A}_i|}\frac{\nabla\alpha_{1,i}}{|\nabla\alpha_{1,i}|}, \quad (3.3)$$

with the parameter $c_\alpha \leq 1$ and the cell face vector $\boldsymbol{A}_i$. Solving (3.2) yields an updated α_1 for the new time t. The partial derivatives are discretised using low order discretisation schemes like the Euler scheme for temporal and the upwind scheme for spatial derivatives. Numerical errors of this solution may result in α_1 being slightly below 1 within the bulk of the liquid. Once such a cell is exposed to a low pressure, we wrongly observe the creation of new gas regions. We overcome this problem by a correction of α_i, i.e. cells with a value

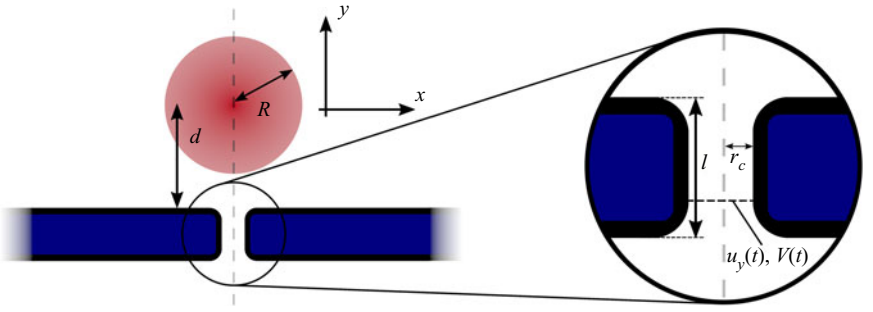

Figure 1. Simulation geometry (not to scale) of a single bubble in the vicinity of a plate with thickness l including bubble radius R and stand-off distance d. The plate is perforated by a channel of radius r_c.

of $\alpha_i > 0.9999$ are clamped to $\alpha_i = 1$. This threshold value was chosen to remove the wrongly created gas regions without significantly affecting the main bubble dynamics.

Next the Navier–Stokes equation (2.2) is solved to update the velocity field $\boldsymbol{u}$. Since gravitational effects are neglected, the volume force term disappears ($\boldsymbol{f} = 0$). The pressure field is computed iteratively, using the pressure-implicit method with splitting of operators (PISO) scheme. For that, the Navier–Stokes equation (2.2) is written as

$$M\boldsymbol{u} = -\nabla p, \tag{3.4}$$

where M is a known tensor. Now the diagonal elements of M are defined as A and another quantity $\boldsymbol{H} = (M - A)\,\boldsymbol{u}$ is defined. Then, (3.4) can be written as

$$\nabla(-A^{-1}\nabla p) = A^{-1}\boldsymbol{H} - \nabla \cdot \boldsymbol{u}. \tag{3.5}$$

This is solved to update the pressure field p and from there, the velocity and density fields are corrected. Discretisation errors cause the bubble mass, which is calculated from $m = \sum_i^{cells} \alpha_{2,i}\,\rho_{2,i}\,V_i$, to fluctuate. To counteract this, the density is corrected as $\rho'_{2,i} = (m_0/m)\,\rho_{2,i}$ to keep the bubble mass constant, where m_0 is the initial bubble mass calculated at $t = 0$, as seen in Koch *et al.* (2016).

The updated $\boldsymbol{u}$ and ρ are used to correct p, and are then corrected once again. Finally, the density field ρ is updated using $\rho = \alpha_1\rho_1 + \alpha_2\rho_2$, and the new compressibility fields ψ_1 and ψ_2 are obtained from

$$\psi_j = \frac{1}{\gamma_j(p + B_j)}. \tag{3.6}$$

3.2. *Geometry*

The geometry of interest is axisymmetric. It consists of two cylindrical reservoirs (each with a height of 5 mm and a radius of 5 mm) connected via a thin channel with a common axis of symmetry, as shown in figure 1. Both orifices of the channel are filleted (with a radius of curvature of 25 μm) to avoid numerical instabilities from sharp edges. Because of the symmetry, only half of the geometry shown in figure 1 is calculated in the simulation. The flow equations are solved in the x–y-plane, where the y-axis is the rotational axis of the system. This results in an effectively two-dimensional simulation, which greatly reduces the cost of computation.

Within the OpenFOAM framework, the geometry is reduced to a thin wedge that is thinnest at the y-axis and is only divided into cells along the x- and y-directions.

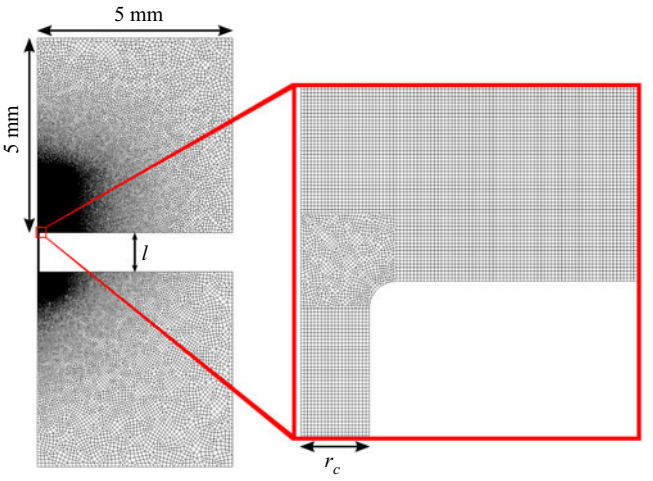

Figure 2. Computational mesh of the channel geometry with $r_c = 50\,\mu\text{m}$ and $l = 1\,\text{mm}$. An unstructured mesh is used far from the bubble and at the filleted channel orifices. Close to the bubble and in the channel, a structured mesh is used.

The geometry is discretised into a square mesh, as seen in figure 2, which close to the location of the bubble is resolved with a cell width of 2.5 µm. Outside of this region of interest, an unstructured mesh is used, where the cell size increases with distance from the bubble to approximately 100 µm width at the outer boundary of the geometry.

3.3. *Initial conditions*

The simulations are started with a small spherical bubble seed on the axis of symmetry with 50 µm radius. The bubble interior is assigned $\alpha = 0$ while the bubble exterior is assigned $\alpha = 1$. The field α is then smoothed by solving the Poisson equation,

$$\alpha' - 4 \times 10^{-11}\,\Delta\alpha' = \alpha, \tag{3.7}$$

where α' denotes the replacement of the initial field α. This smoothing procedure reduces Rayleigh–Taylor instabilities during the early stage of rapid bubble expansion. The parameter is chosen to provide minimum smoothing but a numerically stable bubble surface during the early expansion phase.

The pressure field is set as $p = \alpha\, p_0 + (1 - \alpha)\, p_g$ with the atmospheric pressure p_0 and the initial gas pressure p_g. Here, p_g is chosen such that the density of the gas is equal to the liquid density, $\rho_g = \rho_l$. Using this and the Tait equation (2.3) for the gas, a gas pressure of $p_g = 16.88\,\text{kBar}$ is obtained. This is based on the assumption that for a laser generated bubble, the energy deposition by the laser pulse is much faster than the bubble expansion, so that the liquid seed vapourises almost instantaneously, before the bubble seed expands significantly. Initially, the velocity field is zero in the entire fluid domain.

The simulations were carried out as parallel processes using four CPU cores of an AMD Ryzen Threadripper 1900X at 3.8 GHz each with 64 GB of RAM. The time needed to run a simulation is roughly proportional to the square of the number of cells computed. For this work, the time taken ranged between 21 and 51 h to simulate 200 µs of the bubble dynamics after bubble initiation.

3.4. *Boundary conditions*

In the following, the directions x, y and z in the simulation results are considered synonymous with right, up and front, respectively. The leftmost boundary is imposed with the SYMMETRYPLANE boundary condition for all fields. Similarly, the boundary condition WEDGE is used for the front and back planes of the geometry. The fluid boundaries of the two large fluid regions located at the top, bottom and right in figure 2 represent an infinitely large fluid domain; therefore, their boundary conditions are $p = 10\,1325$ Pa, $\nabla u_i = 0$ and $\nabla\alpha = 0$. The remaining boundary is the one separating the two fluid domains, which also bounds the channel that connects them. This is a rigid wall with a no-slip boundary condition, $\boldsymbol{u} = 0$ and $\nabla p = 0$. There we also impose a boundary condition of $\alpha = 1$. This can be justified to some extent by the experiments of Reuter & Kaiser (2019), who found that a bubble collapsing very close to a wall in water does not touch the wall but is separated from it via a thin liquid film during its first collapse. Their experiments covered the stand-off distances $0.47 < \gamma < 1.07$, $\gamma = d/R_{max}$ here denoting the dimensionless stand-off parameter with the maximum bubble radius R_{max} and the distance between the bubble centre and the wall d. In the present work, we assume this separation of the gas and the wall for the full range of γ values studied. Whether this assumption holds true in an experimental setting may depend on the wettability and structure of the surface. If in such a setting the bubble came into contact with the wall, the contact angle would be expected to play a minor role on the bubble dynamics. Thus, we would still expect the formation of the main jet causing the pumping effect.

4. Experimental setup

The experiments use a laser-induced bubble in front of a perforated boundary. A schematic representation of the setup is shown in figure 3. It consists of a glass tank with dimensions 55 mm × 55 mm × 65 mm filled with deionised water. A microscope objective (Mitutoyo × 50 Plan Apochromat Objective, 436–656 nm, 0.55 NA, 13 mm WD) is sealed water-tight and incorporated into the bottom of the tank. This objective focuses a Nd:YAG laser pulse (Litron Nano SG-100-2; $\lambda = 532$ nm; FWHM = 6 ns, pulse energy $\approx$ 5 mJ) into the water to seed the bubble. A smaller L-shaped cuvette that accommodates a plate with a micro-perforation is submerged into the glass tank connected to a motorised three-axis stage. The plate is made out of a flexible polymeric material used for printed circuit boards (supplier: PCBWay). It has dimensions of 16 mm × 12 mm × 170 µm. The perforation is a cylindrical drilled hole of 195 µm in diameter (measured with a light microscope). The bubble is produced axially in front of the perforation which is confirmed by a high-speed camera with a perpendicular view on the plate surface (Photron FASTCAM MINI AX200). To avoid the generation of spurious bubbles on the plate, which can happen as the laser energy is not entirely absorbed in the plasma, the laser is focused in parallel to the plate. This implies a partial blocking of the focusing cone that is dependent on the stand-off distance. To assure constant maximum bubble size over all stand-off distances, half of the laser beam is blocked at the input aperture side of the objective.

To visualise the pumping effect of the bubble, the L-shaped cuvette is filled with an aqueous 3 wt% NaCl solution which results in optical Schlieren at the mixing interface. Schlieren high-speed imaging is implemented to visualise the transport of two nearly identical liquids. For that, the water tank is illuminated by a collimated pulsed laser beam (Ekspla FemtoLux 3; λ = 515 nm; 1 MHz) parallel to the plate. After passing the tank, the light gets focused by an objective where the undeflected part is blocked by a knife edge and the deflected light is directed into a second high-speed camera (Shimadzu Hyper Vision

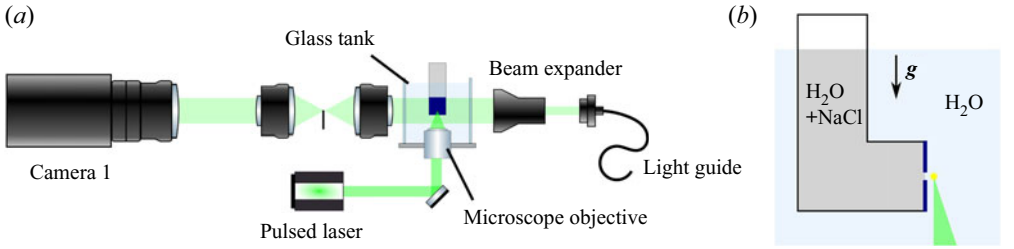

Figure 3. Schematic experimental setup (not to scale): (*a*) optical path for bubble generation as well as Schlieren imaging through the glass tank; (*b*) cuvette with a perforated plate in side view submerged in the glass tank and position of bubble generation.

HPV-X2; camera 1 in figure 3, operated at 500 000 frames per second; shutter opening time 1 µs; effective exposure time 0.3 ps; 7.8 µm pixel^{-1}). The imaging is also sensitive to density changes in the liquid from shock waves which are emitted during the creation and the collapse of the bubble and reflected at the boundaries.

5. Results

We start by demonstrating the effect of the presence of the channel in the rigid boundary on the bubble dynamics via simulations.

5.1. *Jetting through the perforated boundary*

Figure 4 compares the axisymmetric fluid dynamics of a bubble expanding and collapsing close to a rigid wall with an identical bubble close to a perforated wall. The bubble is seeded at a stand-off distance of 500 µm and reaches a maximum radius of approximately 475 µm. This gives a dimensionless stand-off distance of $\gamma = 1.05$. The cylindrical channel has a radius of 50 µm and a length of 1 mm, which is the same as the thickness of the wall separating the two fluid domains. In both cases, the bubble expands and then collapses, creating a jet towards the wall. As a result, the bubble re-expands as a torus close to the wall.

There are small but noticeable differences between the bubble dynamics in the two geometries. In the case with the hole, during the shrinking phase, a small indentation on the lower side of the bubble develops, which is not present in the continuous wall case. This feature is caused by the axial inflow from the opposing fluid domain through the channel and onto the lower bubble wall. The flow deforming the bubble is driven by the pressure difference during the shrinking phase of the bubble, i.e. the low pressure in the bubble and the atmospheric pressure far from the bubble below the boundary.

Overall, both bubbles form a jet starting from the wall-distant pole of the bubble. After this jet has pierced the lower bubble wall, in the continuous wall case, we find a stagnation point at the wall on the axis of symmetry. Further outside, a radially spreading flow along the continuous wall is formed. In contrast, in the perforated wall case, the stagnation point flow is lost and the liquid flows through the hole in the boundary. Viscous stresses oppose the flow through the boundary and some of the jet flow still feeds into the radially spreading flow along the wall. Overall, we find that for these particular chosen parameters, a rather small effect of the perforation on the familiar bubble shape or timing of the bubble dynamics during expansion and collapse is observed, albeit there is a fluid transport occurring through the plate.

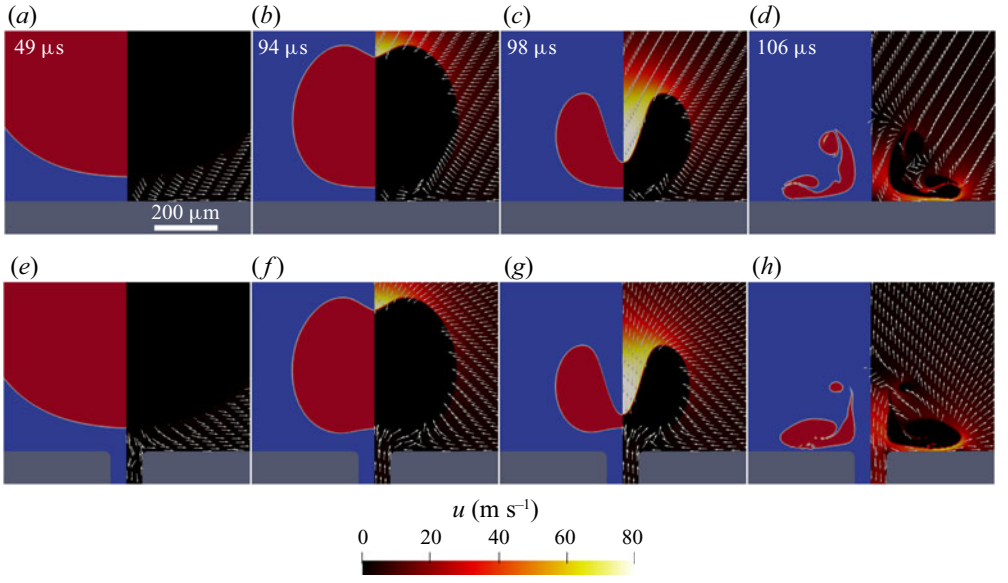

Figure 4. Simulations of a cavitation bubble close to a rigid boundary with stand-off parameter $\gamma = 1.05$, comparison of the flow dynamics for a boundary without (*a–d*) and with a channel below the bubble (*e–h*). The left side of each frame shows the bubble gas in red and water in blue, the right side shows the velocity field in the liquid.

To quantify this pumping effect of the bubble, the liquid flow velocity u_y through the channel outlet, i.e. on the plate surface facing away from the bubble, is measured (just above the rounded edge, see figure 1) and averaged over the channel cross-section as $u_y = (1/\pi r_c^2) \int_0^{r_c} \alpha_1 \boldsymbol{u}_y(r) \cdot \boldsymbol{e}_y \cdot 2\pi r \, \mathrm{d}r$. The result is plotted in figure 5(*a*). Here, a positive sign of u_y indicates a flow from the bottom water reservoir to the top and a negative sign, a flow in the downward direction. The red line in figure 5 depicts the volume equivalent bubble radius R to help the reader to link the bubble dynamics to the channel flow. Figure 5(*a*) shows that during bubble expansion, the liquid is initially accelerated downwards to approximately $u_y = -10\,\mathrm{m\,s^{-1}}$ before the velocity reduces to approximately 0 at the time of maximum bubble expansion ($t = 50\,\mu\mathrm{s}$). Then, rather symmetrically, the liquid is transported in the opposite direction and slowly accelerated during bubble shrinkage. Just prior to the collapse, a rapid acceleration sets in, reverting the flow direction and accelerating it to approximately $u_y = -18\,\mathrm{m\,s^{-1}}$ at $t = 105\,\mu\mathrm{s}$. At this time, the jet has developed and pushes the liquid through the channel. Examining the bubble dynamics between $t = 100\,\mu\mathrm{s}$ and $t = 200\,\mu\mathrm{s}$, we find a second oscillation cycle of the bubble with a reduced equivalent bubble radius. We want to remind the reader that the bubble is not spherical but has now transformed into a toroidal shape. While the fluid velocity u_y is rather symmetrical for most of the expansion and shrinkage of the first bubble oscillation, i.e. downward during bubble expansion and upward during shrinkage, we see a different feature during the second oscillation cycle. Here the velocity u_y remains negative for most of the second oscillation cycle and the flow reverses only shortly before the second collapse. As a consequence, we can expect that a net downward flow occurs during this part of the bubble oscillation. This expectation is confirmed in figure 5(*b*). It plots the liquid volume V transported through the channel as a function of time, which is calculated as $V(t) = \pi r_c^2 \int_0^t u_y(t') \, \mathrm{d}t'$. Again, a negative sign stands for a net liquid

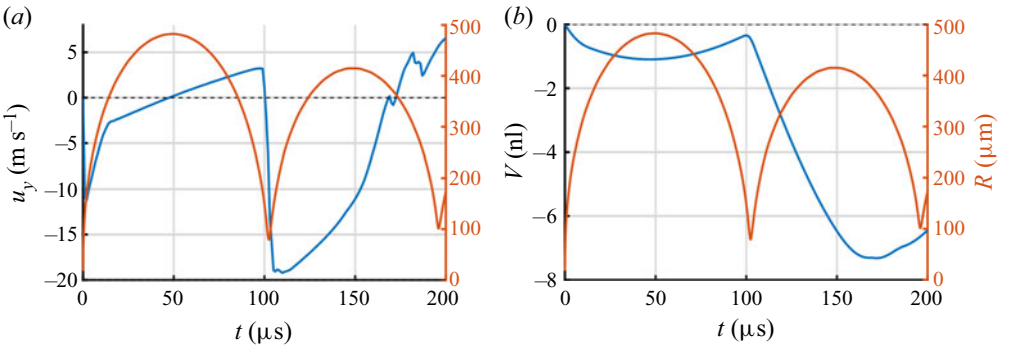

Figure 5. (*a*) Velocity u_y at channel exit (near the solid surface facing away from the bubble) and (*b*) liquid volume $V(t)$ transported through the channel, each overlaid with the bubble radius R to show the correlation between the bubble dynamics and the flow through the channel.

transport downwards through the channel. Figure 5(*b*) shows a roughly symmetrical flow during the first oscillation period as discussed above, pumping liquid downwards during bubble expansion and upwards during bubble shrinkage. The cumulative volume flow V remains negative for this entire oscillation cycle. Upon bubble collapse, the developed jet creates a strong downward flow through the channel, which lasts until the maximum expansion of the second bubble oscillation cycle and reaches up to 7 nL at 170 µs, before the flow is reversed and the net amount of pumped liquid is slightly reduced. It is instructive to compare the pumped liquid with the maximum bubble volume, which is approximately 500 nL, and with the volume of the channel, which is approximately 8 nL.

5.2. *Variation of parameters*

The present fluid transport problem is rich in the choice of parameters, e.g. the geometry of the channel (length l, radius r_c, shape), the stand-off distance d of the bubble and the properties of the liquid, to name a few. In this section, we vary some of these parameters individually and document their effect on the pumped liquid through the channel. The flow behaviour in the channel in tandem with the evolution of the bubble radius R observed in figure 5 happens in a similar fashion in all the following cases studied, meaning that the first bubble collapse is accompanied by the formation of a microjet towards the perforated plate and a sudden acceleration to a high magnitude negative flow velocity u_y in the channel.

5.2.1. *Variation of the channel length*

The three channel lengths, $l = 200$ µm ($= 0.42\ R_{max}$), $l = 400$ µm and $l = 1000$ µm ($= 2.11 R_{max}$), are studied. The main difference caused by this change is the viscous flow resistance of the channel flow. As a result, for shorter channels, we observe higher flow velocities u_y (see figure 6(*a*) at $t = 110$ µs), yet the duration of the flow driven by the liquid jet is also shorter. This is because after the first collapse, the inertia of the liquid jet transports gaseous fragments of the bubble along and through the channel. Once the bubble content reaches the lower end of the channel (where the liquid flow is measured), the liquid flow rate abruptly diminishes, which happens at approximately $t = 110$ µs for $l = 200$ µm and $t = 120$ µs for $l = 400$ µm. Also, for shorter channels, a stronger backflow towards the collapsing bubble is created (approximately $t = 150$ µs), which affects and reduces the net flow further. This is due to the second bubble collapse,

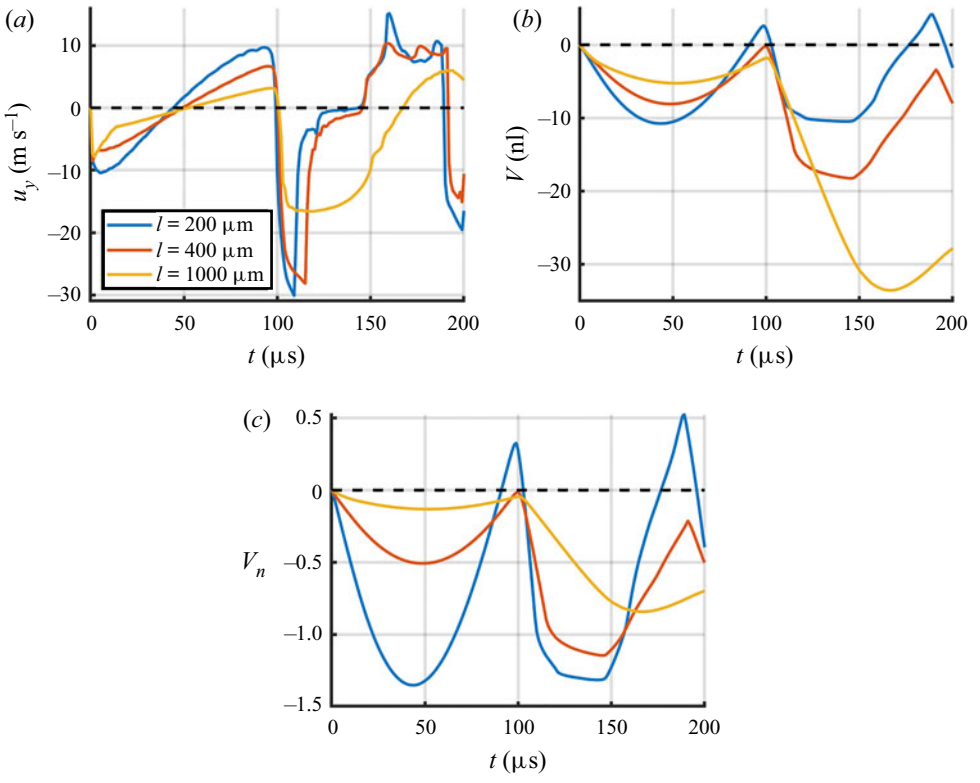

Figure 6. Study of the liquid transport as a function of the length of the channel l for $r_c = 112.5\,\mu\text{m}$, $d = 500\,\mu\text{m}$, $R_{max} = 475\,\mu\text{m}$: (*a*) velocity $u_y(t)$ at channel exit; (*b*) liquid volume $V(t)$ transported through the channel and (*c*) transported liquid volume normalised by the channel volume $V_n(t)$.

when the channel begins to fill with liquid from the bottom again. During the third expansion (starting at approximately $t = 180\,\mu\text{s}$), the liquid is pushed downwards through the channel again. For $l = 200\,\mu\text{m}$, similar amounts of liquid are being moved up and down through the channel, creating a roughly periodic pattern in the volume transport curve $V(t)$ in figure 6(*b*). The bubble dynamics for short channels is discussed in greater detail during the comparison with the experiments, see § 6.2. Since the transported liquid volume V increases with increasing channel length l, one may suspect that the transported volume scales with the channel volume ($\sim l$). Therefore, we plotted the transported liquid volume normalised by the channel volume, $V_n(t)$, in figure 6(*c*). This reveals that $V(t)$ does *not* scale with the channel length l and relatively smaller liquid volumes are pumped for longer channels.

5.2.2. *Variation of the channel radius*

Next the radius of the channel r_c is varied between 25 µm (or 0.05 R_{max}) and 200 µm (or 0.42 R_{max}). Figure 7(*a*) shows that for thinner channels, the liquid jet causes a higher velocity u_y, yet for a shorter duration compared to the wider channels (see $100\,\mu\text{s} \leq t \leq 150\,\mu\text{s}$). Similar to § 5.2.1, the faster decay in fluid velocity can be attributed to the stronger viscous drag in the thinner channels. For wider channels, an increasingly larger part of the bubble moves into the channel after collapse. In the case of $r_c = 200\,\mu\text{m}$, the bubble collapses downwards after the second expansion, entirely entering the channel. This stands

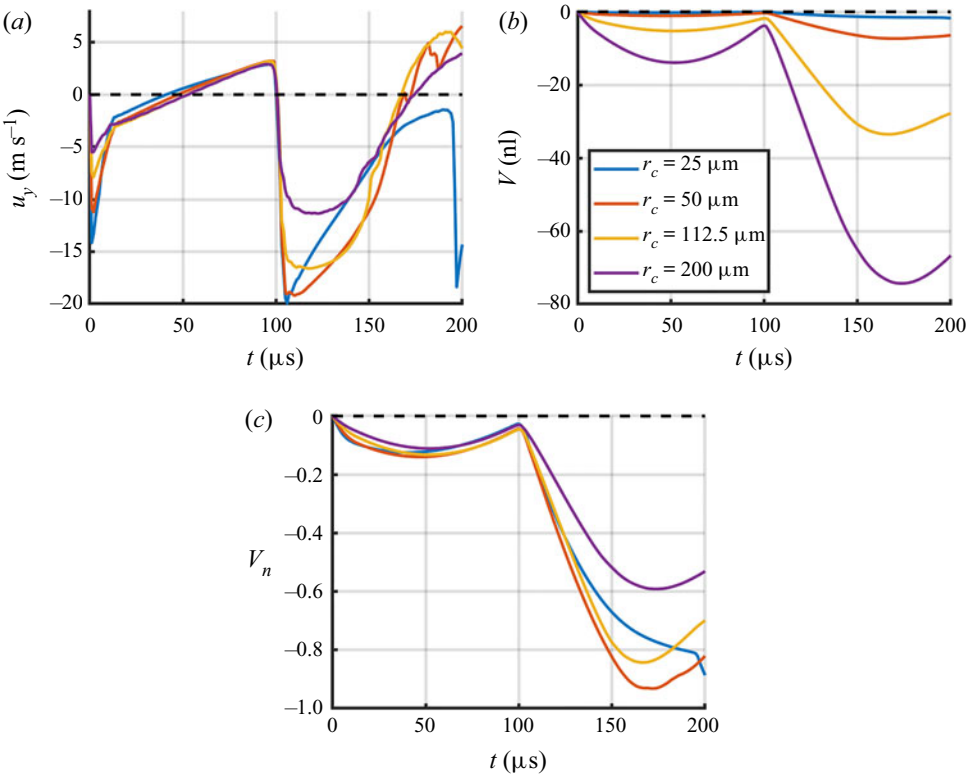

Figure 7. Study of the liquid transport as a function of the radius of the channel r_c for $l = 1000\,\mu\text{m}$, $d = 500\,\mu\text{m}$, $R_{max} = 475\,\mu\text{m}$: (*a*) velocity $u_y(t)$ at channel exit; (*b*) liquid volume $V(t)$ transported through the channel and (*c*) transported liquid volume normalised by the channel volume $V_n(t)$.

in contrast to the previous cases, where the second bubble collapse is directed towards the axis of symmetry. The larger cross-sections allow a much larger liquid flux to pass through them compared to thinner channels (see figure 7*b*). If the flow velocity u_y is almost unaffected by the channel width, which it is at least until the bubble collapse, we expect the transported volume V to scale with the channel volume ($\sim r_c^2$). This is indeed supported by figure 7(*c*), where the normalised transported liquid volume V_n during the first bubble oscillation is approximately the same for each r_c. Yet, after jetting, V_n is affected by the channel radius r_c and reaches the largest magnitude value for $r_c = 50\,\mu\text{m}$.

5.2.3. *Variation of the channel shape*

The channel shape is varied by fixing the radius at the upper end of the channel at $r_{c,upper} = 50\,\mu\text{m}$ and changing the radius at the lower end to $r_{c,lower} = 25\,\mu\text{m}$ to obtain a narrowing channel, and $r_{c,lower} = 100\,\mu\text{m}$ for a widening channel. The ends are connected via a straight line, creating channels of a truncated cone geometry. Figure 8(*d*) schematically depicts these three channel shapes. In the narrowing channel, a higher absolute pumping velocity is reached, as seen in figure 8(*a*). For the widening channel, a higher amount of fluid is transported through them (while the channel volume also increases), as seen in figure 8(*b*), but there is also a stronger backflow that acts against the net amount of fluid pumped downwards through the channel, see figure 8(*b*) at $150\,\mu\text{s} \leq t \leq 200\,\mu\text{s}$. Plotting the transported liquid volume divided by the respective channel volumes, V_n,

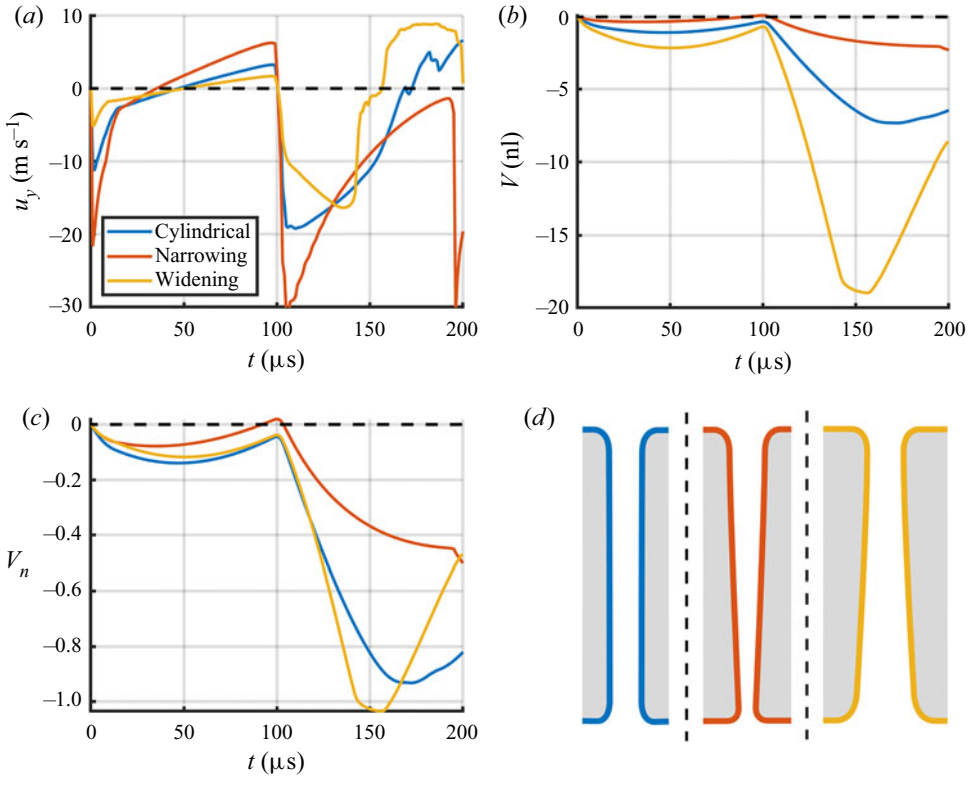

Figure 8. Study of the liquid transport as a function of the shape of the channel for $r_{c,upper} = 50\,\mu\text{m}$, $l = 1000\,\mu\text{m}$, $d = 500\,\mu\text{m}$, $R_{max} = 475\,\mu\text{m}$: (*a*) velocity $u_y(t)$ at channel exit; (*b*) liquid volume $V(t)$ transported through the channel; (*c*) transported liquid volume normalised by the channel volume $V_n(t)$ and (*d*) schematic of channel shapes used.

reveals that the cylindrical channel transports the largest absolute volume over the first 200 µs (see figure 8*c*).

5.2.4. *Variation of the liquid viscosity*

Next we increase the viscosity of the liquid from that of water ($\mu = 1$ mPa s) by 1 and 2 orders of magnitude, respectively, while keeping the gas viscosity constant. Figure 9 summarises the results and reveals the expected drastic decrease of the absolute pumping velocity u_y and pumped volume V, as well as a stronger damping of the flow in the channel. Interestingly, the backflow towards the bubble is strongly reduced for $\mu = 100$ mPa s. This can be attributed to the strong viscous damping of the microjet. Unlike in the cases with lower viscosity, the jet drags no bubble gas into the channel that would create a backflow during the collapse later. The viscous damping also causes the bubble to have a 37 % larger collapse time during its first oscillation and reach a 42 % smaller rebound volume upon its second expansion than in the case of $\mu = 1$ mPa s. In Appendix B, we estimate the total pumped volume as a function of the viscosity (B5) assuming a dissipating Hagen–Poiseuille flow. From that consideration, neglecting the effect of viscosity on the jetting, the pumped volume can be considered to be proportional to r_c^4 and μ^{-1}.

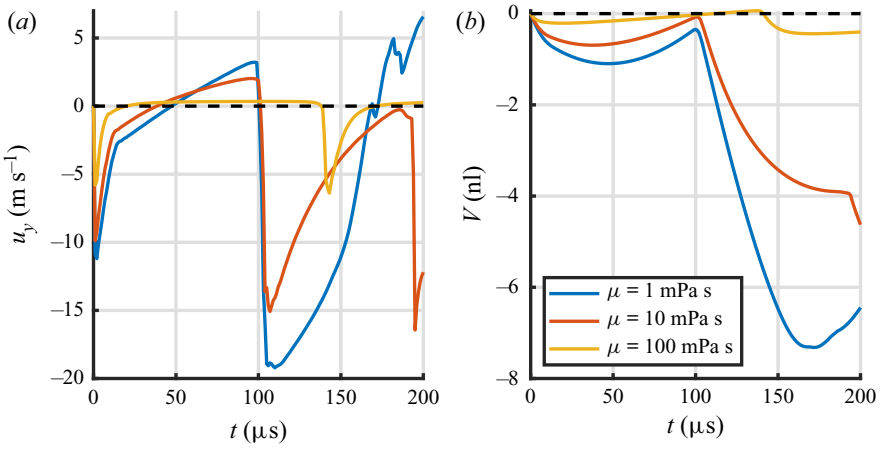

Figure 9. Study of the liquid transport as a function of the liquid viscosity μ for $r_c = 50\,\mu$m, $l = 1000\,\mu$m, $d = 500\,\mu$m, $R_{max} = 475\,\mu$m: (*a*) velocity $u_y(t)$ at channel exit and (*b*) liquid volume $V(t)$ transported through the channel.

5.2.5. *Variation of the stand-off distance*

Increasing the stand-off distance of the bubble seed from $d = -50\,\mu$m ($\gamma = -0.11$) up to $d = 750\,\mu$m ($\gamma = 1.58$) reveals a general trend that the velocity u_y and the amount of liquid pumped V decreases with the distance (see figure 10*a*). For the smallest distances d, considerably higher velocities of up to $u_y = -55\,\mathrm{m\,s^{-1}}$ at $d = -50\,\mu$m are achieved, yet these distances also result in a stronger backflow during the second bubble oscillation period. This can be partly attributed to the bubble expanding into the channel after jet formation, pushing liquid down through it and dragging liquid up again during the subsequent collapse. Overall, the highest pumped volume through the channel V is achieved for the smallest distances d (see figure 10*b*). For large distances, i.e. $d = 750\,\mu$m, a net pumped volume of nearly zero is observed just prior to the first bubble collapse. This behaviour is expected for an inviscid, spherically oscillating bubble that does not translate, i.e. one that can only be fulfilled for large stand-off distances. Interestingly, the decrease in peak velocity and pumped volume up to the second collapse is not a monotonic function of d but contains a local maximum around $d = 500\,\mu$m ($\gamma = 1.05$, see figure 10*a* at $t = 105\,\mu$s and 10*b* at $t = 170\,\mu$s). The bubble dynamics changes significantly as a function of the stand-off distance d. As the bubble is generated closer to the boundary, it becomes more deformed from a spherical shape until it obtains an almost hemispherical shape at maximum expansion with a small protrusion reaching into the perforation in the boundary. In the case of $d = 100\,\mu$m, no pronounced jetting is visible, instead an annular flow develops in the late stage of an almost hemispherical collapse. This flow interacting with the late microjet from above compete and mitigate jetting. For $d = 0$, the bubble develops a considerably thinner jet that, due to its higher speed, pulls along gas from the bubble into and through the channel during bubble re-expansion. This change in jetting behaviour is discussed in greater detail in the following section. Figure 10(*c*) shows that for $d < 0$, the velocity peak is reached at a later time, which can be linked to the bubble expanding further into the channel. There, the gas phase collapses only after a few microseconds after the collapse of the main bubble (see figure 11 at 103.0 µs).

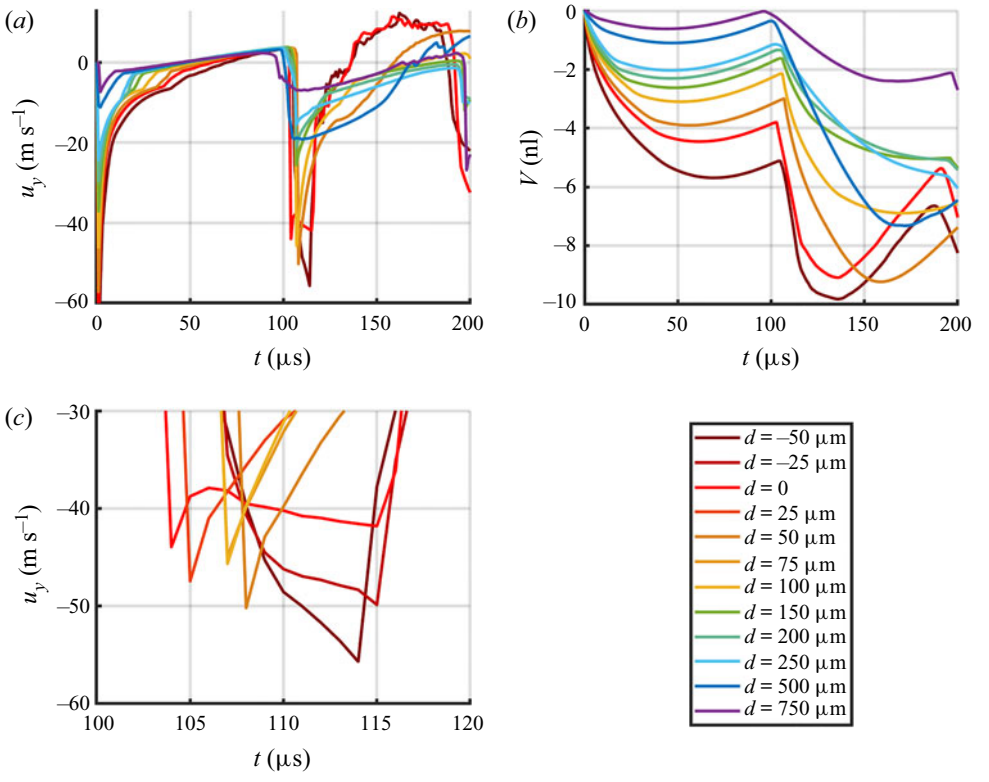

Figure 10. Study of the liquid transport as a function of the stand-off distance d for $r_c = 50\,\mu\text{m}$, $l = 1000\,\mu\text{m}$, $R_{max} = 475\,\mu\text{m}$: (*a*) velocity $u_y(t)$ at channel exit; (*b*) liquid volume $V(t)$ transported through the channel and (*c*) velocity $u_y(t)$ at channel exit after jetting for $d = -50 \ldots 100\,\mu\text{m}$.

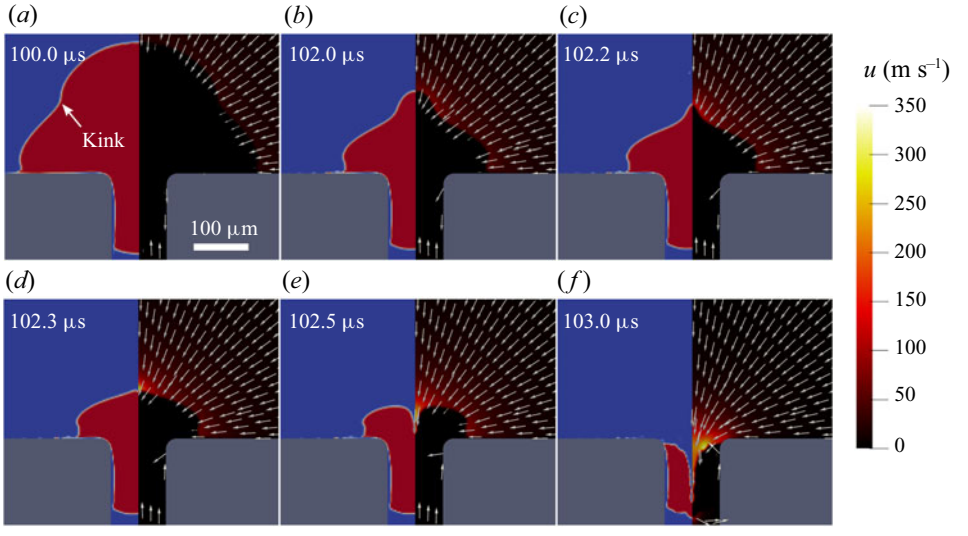

Figure 11. Simulation of cavitation bubble dynamics in the perforation of a rigid plate in the plane of the upper wall of the plate ($\gamma = 0$). The left side of each frame shows the bubble gas in red and water in blue, the right side shows the velocity field in the liquid.

6. Selected pumping regimes

After studying the pumping effect and the influence of parameters thereon in the preceding sections, we now examine the effect of the channel on the bubble dynamics for two distinct regimes in greater detail.

6.1. *Needle jet regime: small stand-off distance and long channel*

Figure 4 reveals that for $\gamma \approx 1$, the shape of the bubble near a plane, unperforated boundary is rather similar to the shape observed near one which is perforated with a long and slender hole ($l = 1$ mm, $r_c = 50\,\mu$m). When the bubble is generated very close to an unperforated boundary, the jetting behaviour of the bubble transitions from the commonly known rather wide jets to a considerably thinner and faster jet, termed *fast, thin jet* (see Lechner *et al.* 2020) or *needle jet* (see Reuter & Ohl 2021) that can reach a velocity with an order of magnitude of 1000 m s^{-1}, as revealed in simulations and experiments. We want to address the question whether this needle jet may also occur at a perforated boundary. With a hole in the boundary, the bubble can be initiated even closer and even within the channel, offering the possibility to probe negative stand-off distances. Figure 11 shows a bubble initiated on the boundary ($\gamma = 0$), where the bubble penetrates into the perforation during expansion. There, the upper part of the bubble obtains an approximately hemispherical shape and the lower takes on that of a cylinder filling the cross-section of the hole. As it starts to collapse, a circular kink forms at the upper part of the bubble ($t = 100.0\,\mu$s). As the bubble shrinks, the kink remains roughly at the same distance from the wall, yet it converges in diameter (see $t = 102.0\,\mu$s and $t = 102.2\,\mu$s in figure 11). This has been connected with a wall-parallel radially convergent inflow focusing on the axis of symmetry (Lechner *et al.* 2020). Upon impact, this focused flow is responsible for the acceleration of liquid in the shape of a needle to high speeds along the axis of symmetry (see $t = 102.3\,\mu$s, $t = 102.5\,\mu$s and $t = 103.0\,\mu$s in figure 11). Please note that in addition to the prominent downward needle-like jet flow, in the perforation, a flow upwards is also created that competes against the spherically convergent main flow. The very thin downwards jet pierces the bubble with a velocity of 367 m s^{-1}, whereas the commonly known jet flow of a bubble at larger stand-off distances does not exceed approximately 100 m s^{-1}. It is important to note that the velocity of the fast jet is strongly dependent on the grid size, as reported by Lechner *et al.* (2020), and thus may here be underestimated. The present observation shown in figure 11 resembles the bubble dynamics reported by Lechner *et al.* (2020) and confirms that a needle jet can occur in the presence of a perforated boundary too.

The emergence of the needle jet phenomenon with decreasing γ is easily revealed by plotting the maximum of the absolute velocity of the entire liquid domain, u_j, and the radius of the jet r_j in figure 12(*a*,*b*). Following the curves from large γ-values to smaller γ in figure 12(*a*), the velocity of the liquid jet u_j decreases slowly at first from approximately 100 m s^{-1} and then sharply rises to values of several 100 m s^{-1}, showing the lowest value at $\gamma = 0.3$.

The radius of the jet r_j is defined as the radius of the widest column along the axis of symmetry that is entirely filled with liquid after the jet has pierced the bubble (see figure 12*b*). This jet radius r_j reveals a maximum at $\gamma = 0.5$ but sharply drops to a very low value for $\gamma \lesssim 0.2$. Here, the jet becomes so thin that it is not fully resolved in the present simulations and splits into small droplets without fully penetrating the bubble. Then, a jet radius of $r_j = 0$ is plotted in figure 12(*b*).

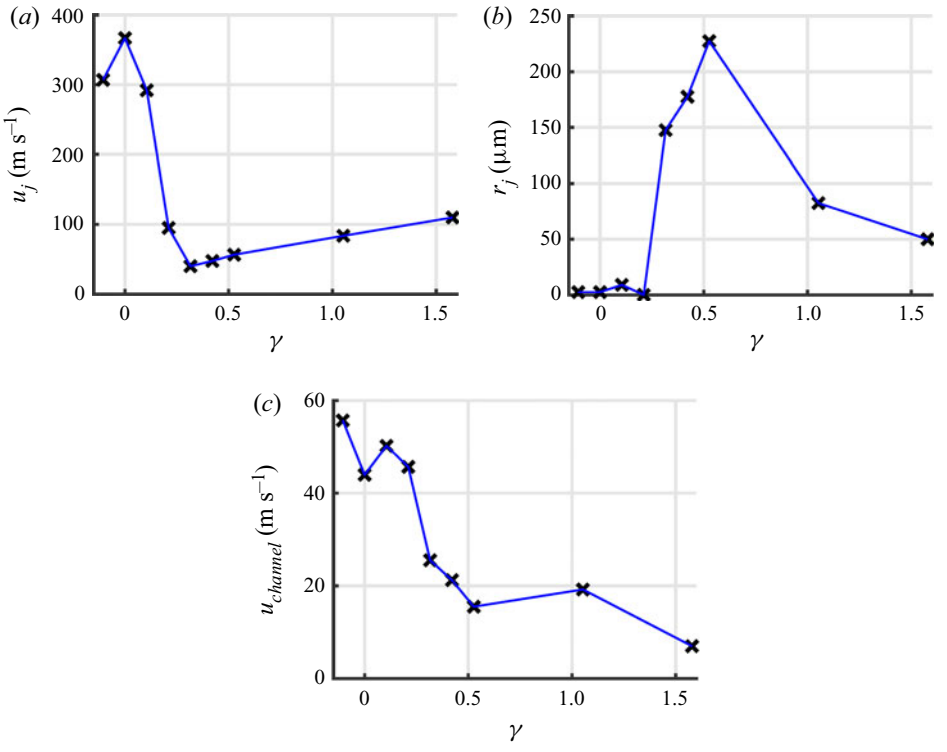

Figure 12. Study of the transition between jet and needle jet as a function of the normalised stand-off parameter γ: (*a*) jet velocity $u_j(\gamma)$; (*b*) jet radius $r_j(\gamma)$ and (*c*) maximum flow velocity at the channel exit $u_y(\gamma)$.

The velocity produced at the lower end of the channel u_y (see figure 12*c*) shows a pronounced rise for $\gamma < 0.5$; however, it is not as abrupt as during the formation of the needle jet. Judging from these results, the needle jet occurs at $\gamma \lesssim 0.2$, while the standard jet occurs at $\gamma \gtrsim 0.5$, with a transition region between $\gamma = 0.2$ and $\gamma = 0.5$, where no needle jet occurs, but the jetting behaviour changes.

6.2. *Reverse jet regime: small stand-off distance and short channel*

Next we investigate the bubble dynamics close to a short channel ($l = 170\,\mu$m). We chose this regime because in the experiments, both sides of the plate can be captured by a single camera in the case of a thin plate. A second motivation was the report of a jet directed away from the wall by Cui *et al.* (2013) that formed only near thin perforated plates which is also absent for unperforated walls. In this regime, we provide two comparisons between the simulated flow and the experiment in figure 13 with a stand-off distance of $d = 108\,\mu$m and figure 14 with $d = 202\,\mu$m. In these figures, on the left and on the right, the simulated bubble and the experiment are depicted, respectively. We present not only the shape but also the transported liquid using a digital ink map in the simulations to visualise the net fluid transport from the unsteady flow field of cavitation bubbles as introduced by Reuter *et al.* (2017). This passive tracer field of different colours is advected with the simulated flow field. Initially, the liquid in the upper reservoir is coloured black and that in the lower with a bright grey. Additionally, the liquid in the perforation is coloured continuously from the top to the bottom from black to red to yellow to bright

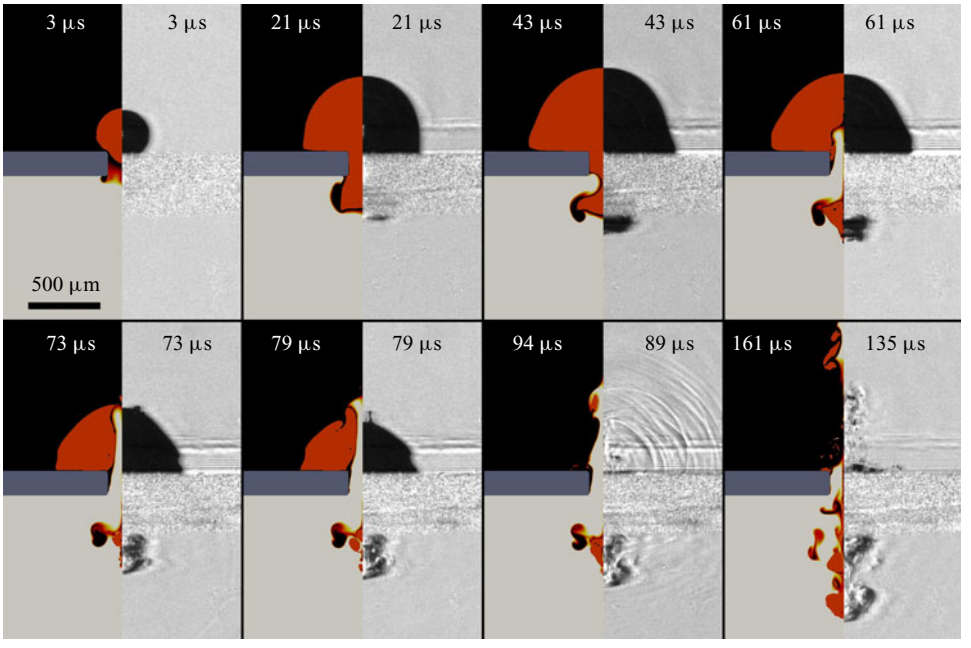

Figure 13. Comparison between simulation (left) and experiment (right) of a cavitation bubble of maximum radius $R_{max} \approx 460\,\mu\text{m}$ at distance $d = 108\,\mu\text{m}$ from a perforated wall, $l = 170\,\mu\text{m}$, $r_c = 97.5\,\mu\text{m}$. Bubble is shown in red, ink map of the liquid above the channel in black, liquid below the channel in white.

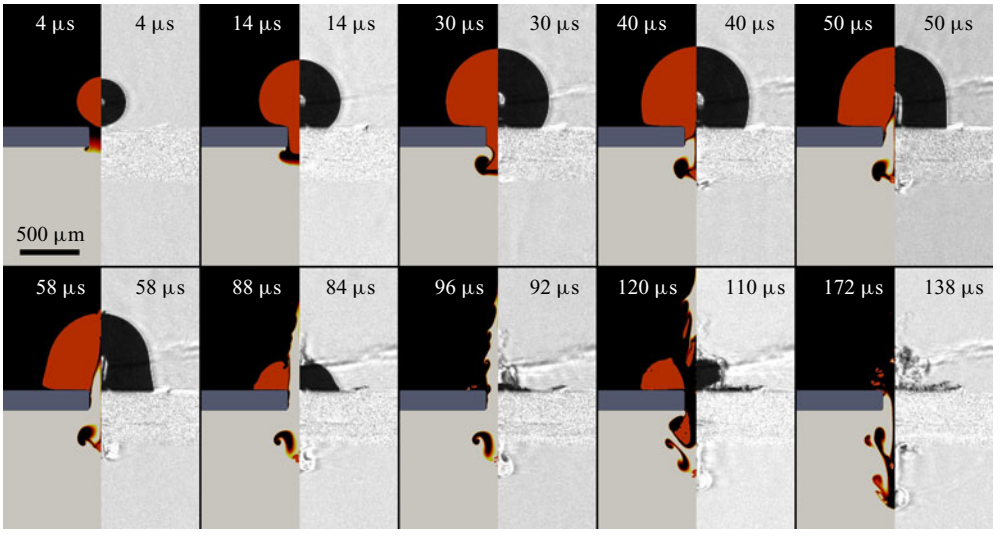

Figure 14. Comparison between simulation (left) and experiment (right) of a cavitation bubble of maximum radius $R_{max} \approx 460\,\mu\text{m}$ at distance $d = 202\,\mu\text{m}$ from a perforated wall, $l = 170\,\mu\text{m}$, $r_c = 97.5\,\mu\text{m}$. Bubble is shown in red, ink map of the liquid above the channel in black, liquid below the channel in bright grey.

grey at the bottom. Adding the ink map, we can not only depict the bubble shape but also the origin of liquid at a later stage during the pumping. For example, the black blob in the lower reservoir in the simulation part of figure 13(*a*) is liquid that has been pumped from the upper into the lower reservoir.

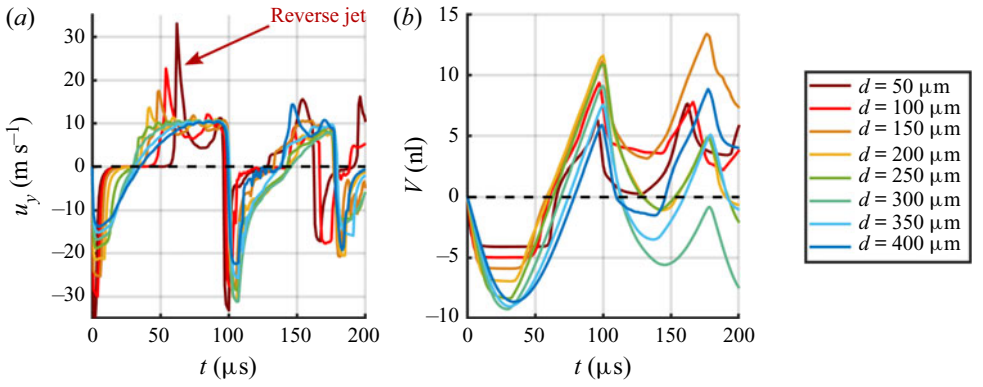

Figure 15. Study of the liquid transport as a function of the stand-off distance d for $r_c = 97.5\,\mu$m, $l = 170\,\mu$m, $R_{max} = 475\,\mu$m: (*a*) velocity $u_y(t)$ at channel exit and (*b*) liquid volume $V(t)$ transported through the channel.

The experiment uses the higher index of refraction of the aqueous NaCl solution to visualise liquid transport via Schlieren imaging. This allows for contrasted high-speed recordings in regions of liquid entrainment. Note that due to the optical configuration, the liquid leaving the channel at the lower side can only be observed once it has propagated approximately 310 μm downwards into the bulk.

We start the discussion with the simulated bubble dynamics for a rather small stand-off distance of $d = 108\,\mu$m ($\gamma = 0.23$), as shown in figure 13. In this regime, in the case of an unperforated boundary, a needle jet is observed (see § 6.1) as well as when the boundary is perforated with a long channel. However, in the presence of a short channel, different dynamics is observed. During early bubble expansion ($t = 3\,\mu$s), some of the liquid from the upper reservoir is pushed through the hole into the lower reservoir. This liquid is visible as a small black and coloured blob below the boundary. During the later expansion of the bubble ($t = 21\,\mu$s), a small part of the bubble invades through the hole into the lower reservoir. The two parts of the bubble are now exposed to different flow fields. While the upper mostly hemispherical part of the bubble continuously expands to a maximum size at $t = 43\,\mu$s, the lower part pinches off from the main bubble near the exit of the hole. The stagnation pressure from this pinch-off drives a liquid jet back through the hole into the upper part of the bubble (see $t = 61\,\mu$s in figure 13). This *reverse jet* then impacts at the apex of the upper bubble and eventually injects liquid from the lower reservoir into the upper one at $t = 79\,\mu$s. A careful inspection reveals that the upper hemispherically shaped bubble develops a kink approximately 100 μm from the surface, starting from $t = 73\,\mu$s. The location of the kink converges towards the axis of symmetry at $t = 79\,\mu$s. Yet, the reverse jet prevents a further convergence of this annular flow towards the axis of symmetry. The main bubble collapses at $t = 94\,\mu$s, while the pinched-off bubble in the lower reservoir already collapses at approximately $t = 73\,\mu$s. The pinch-off ($t = 43\,\mu$s) of the bubble protruding through the plate creates a complex mixing flow below with vortices and bubble fragments transported deeper into the lower reservoir. Overall, we find a good agreement between experiments and simulations. It is important to note that the bubble in the simulations collapses earlier than in the experiments. While we have no definite proof, a likely explanation is the elastic deformation of the boundary seen in the experiments and not accounted for in the simulation.

A comparison for a larger stand-off distance of $d = 202\,\mu$m is shown in figure 14 ($\gamma = 0.44$). This results in a decreased invasion of the bubble into the lower reservoir during

the bubble expansion as compared to that in figure 13. Consequently, a smaller part of the protuberant bubble is pinched off below the wall in the range of $30\,\mu s < t < 40\,\mu s$. As a consequence, the reverse jet forms a thinner tip that partly breaks up into small droplets at $t = 50\,\mu s$. The vortex flow created upon pinch-off below the wall is more pronounced, which is likely due to a weaker disturbance of the flow by oscillating gas fragments as compared to figure 13.

Further simulations using the same geometry as in figures 13 and 14 reveal the dependence of the pumping behaviour on the stand-off distance d in figure 15. The backflow is clearly visible in the channel velocity u_y as a positive spike occurring prior to the bubble collapse at $t \approx 100\,\mu s$ in figure 15(a). This stronger backflow is mostly due to the rather small channel length (see also figure 6). The highest amount of pumped liquid can be achieved at $d = 300\,\mu m$ or $\gamma = 0.63$ (see figure 15b), which is in contrast to the γ-dependence of the amount of pumped liquid for a longer channel reported in figure 10.

7. Discussion and conclusion

The simulations and experiments in this work present the flow through a perforation in a thin rigid plate produced by a cavitation bubble collapsing in front of the perforated plate. The effect of several geometric and liquid parameters are studied and overall reveal clear trends on the transport of liquid from the bubble side to the opposite plate side, i.e. the pumping of liquid. A longer channel increases the flow resistance and as a result reduces the liquid exchange between the two fluid domains, i.e. not only the pumping of fluid but also the backflow. For increasingly longer channels, the flow increasingly resembles that of a bubble close to an unperforated wall. Mixing of fluids rather than pumping can be achieved with shorter channels. If a part of the bubble penetrates through the perforation during bubble expansion, that part collapses earlier than the main body of the bubble, resulting in an early jetting flow from the lower fluid domain (see figure 6). We have termed the flow as *reverse jet* and confirmed it in experiments (see figures 13 and 14). The experiments use a Schlieren technique to reveal the mixing of rather similar liquids, i.e. water and an aqueous NaCl solution. While for the mixing of two liquids it may find applications, for the unidirectional pumping it should be reduced. This can be done by increasing the channel length such that the bubble does not expand beyond the lower end of the channel.

A straight cylindrical channel results in larger amounts of liquid being pumped as compared to simple sloped channels. Yet we expect that others geometries such that of a Tesla valve (see Forster *et al.* 1995) may reduce the backflow and increase the pumped volume. An optimisation of the geometry is open for future studies. Even without conducting a study, an optimal value of the channel width r_c for the highest amount of pumped liquid is to be expected, since for the extreme cases of $r_c \to 0$ and $r_c \to \infty$, no liquid pumping will occur, i.e. non-perforated wall and spherical bubble collapse with an absence of jetting, respectively. This has been confirmed and narrowed down in the present study. For the regular jet, the jet radius r_j is in the range of $0.1 \ldots 0.5R_{max}$ (see figure 12). Figure 7 shows that for $r_c = 50\,\mu m$ ($\approx 0.1R_{max}$), overall, the highest flow velocities through the channel are reached and the amount of liquid pumped relative to the channel volume reaches a maximum. Thus an optimum in pumping is achieved when the channel radius is similar to the jet radius. Varying the stand-off distance d of the bubble near a long channel ($l = 1\,mm$) reveals two distinct regimes of strong pumping behaviour: one being around $\gamma = 1$, featuring the typical jet, the other at very small

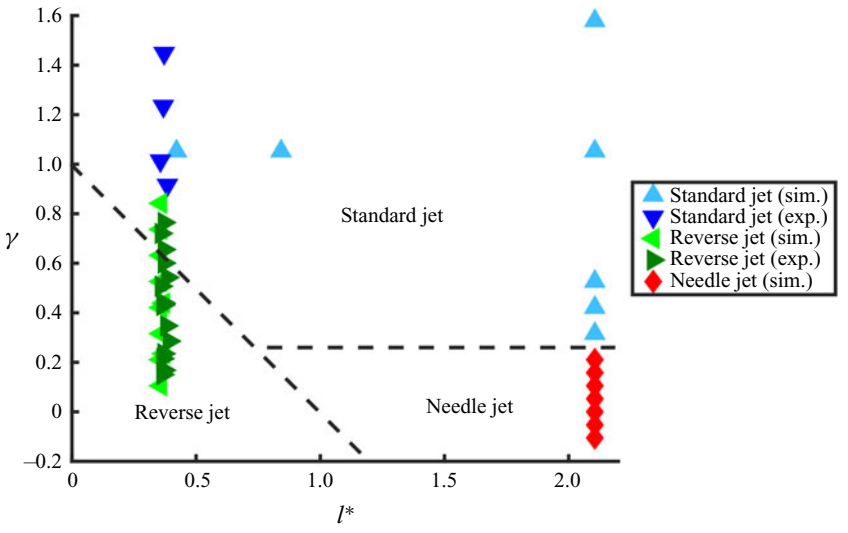

Figure 16. Regime map showing the parameter space of the standard jet, the reverse jet and the needle jet with a dependence on the normalised stand-off distance γ and the normalised channel length $l^* = l/R_{max}$. The dashed lines show $\gamma = 1 - l^*$ and $\gamma = 0.25$.

stand-off distances, where the *needle jet* is observed. This is very similar to the continuous rigid boundary for sufficiently small stand-off distances.

Since the occurrence of the three regimes *reverse jet*, *needle jet* and *standard jet* (jetting without the former two particular jets) depends foremost on the stand-off distance d and the channel length l, we summarise this in the regime map in figure 16. It shows the type of jet formation as a function of the normalised stand-off distance γ and the normalised channel length $l^* = l/R_{max}$ and is collected from simulations and experiments. The reverse jet occurs once a part of the expanding bubble reaches the lower end of the channel. A rough criterion for that to occur is $R_{max} \gtrsim d + l \Leftrightarrow l^* \lesssim 1 - \gamma$, the dashed diagonal line shows $l^* = 1 - \gamma$. Thus, as this line is approached from the standard jet regime, an increasingly stronger backflow occurs. The transition region between the standard jet and the reverse jet spans nearly the entire regime map shown in figure 16. Only for the case $l^* = 2.11$, $\gamma = 1.58$ (data point at the top right of figure 16), the bubble is seeded so far away from the boundary that we cannot detect an effect of the channel on the bubble shape, i.e. the indentation in the lower bubble wall as seen in figure 4(*e–h*) is not formed. The needle jet is only found for $\gamma \lesssim 0.25$ and sufficiently long channels. This region is indicated with the horizontal line in figure 16). For very short channels, the reverse jet and not the needle jet occurs. This is caused by the fact that the reverse jet develops earlier than the main collapse and therefore prevents the annular flow focusing necessary for the needle jet formation. Thus for small l^*, the reverse jet region takes over even if $\gamma \lesssim 0.25$. The simulations presented in this work are limited by the assumption of axisymmetry. This causes noticeable differences compared to the experiments once fragmentation of bubbles or droplets occur. In the simulation, this yields torus-like structures that are unstable in reality (see Reuter & Mettin 2016). Another important limitation is the lack of a phase transition model, which prevents an accurate prediction of the condensation of water vapour present in real cavitation bubbles. Instead, the simulated bubble contains an non-condensable gas that cushions further bubble oscillations. This affects the rebound but also the development of non-axisymmetric instabilities that grow with time.

Therefore, we only show the first 200 µs of bubble dynamics, which includes the first and second bubble collapse only. However, this may have important contributions during the later bubble dynamics. The axisymmetric simulations reveal that not only the first but also successive collapses transport considerable amounts of liquid through the channel. With asymmetries and instabilities as well as energy losses due to condensation influencing the fluid dynamics in reality, we expect less liquid transport than predicted in the simulations.

While understanding the pumping mechanism of viscous liquids was the initial goal, the work could be extended to use the flow below the boundary. This flow affects the strength of the bubble collapse as some of the kinetic energy is used for the transport in the micro-channels. For example, a perforated plate with through-holes that are filled with an immiscible and sufficiently viscous liquid may dissipate some of the kinetic energy and therefore reduce the energy available that is focused during the near boundary bubble collapse. This may reduce cavitation erosion, as was discussed already for perforated plates containing gas (see Gonzalez-Avila *et al.* 2020). Also, we speculate that emulsification of liquids in an ultrasonic bath where two liquids are separated by a perforated plate could benefit from the here found reverse jet. Another point of interest is the jet and spray produced by the bubble if the domain on the opposite side of the perforated wall is filled with a gas instead of a liquid. Potential applications include needleless micro-injections via a fast liquid jet in air and jet-based printing.

Supplementary material and movies. Videos of the numerical and experimental results as well as the code of the numerical solver CavBubbleFoam and an example simulation case can be found as supplementary material to this article.

Supplementary material and movies are available at https://doi.org/10.1017/jfm.2022.480.

Acknowledgements. We are thankful for the discussions with M. Koch, C. Lechner and Q. Zeng on details of the solver in OpenFOAM. Also the help from F. Denner is gratefully acknowledged. We thank R. Mettin for lending some of the laser equipment.

Funding. This work was funded by the German Research Foundation (Deutsche Forschungsgemeinschaft, DFG) under contract OH 75/4-1.

Declaration of interests. The authors report no conflict of interest.

Author ORCIDs.
Hendrik Reese https://orcid.org/0000-0001-8622-1856;
Robin Schädel https://orcid.org/0000-0002-1704-5315;
Fabian Reuter https://orcid.org/0000-0002-8908-4209;
Claus-Dieter Ohl https://orcid.org/0000-0001-5333-4723.

Appendix A. Verification of the simulations

Figure 17(*a*) shows a comparison between the Volume-of-Fluid simulation of a freely oscillating (unbound) bubble and the prediction of the Keller–Miksis equation with equal maximum bubble radius $R_{max} = 470\,\mu\text{m}$. It was done for a geometry of dimensions 100 mm × 50 mm, which is tenfold larger than what was used for the rest of this work to avoid shock wave reflections at the outer boundaries of the simulation geometry. It shows excellent agreement for the first oscillation period. Since the collapse of the bubble in the VoF simulation is not perfectly spherical due to asphericities in the geometry and the mesh grid, its second oscillation period shows a weaker expansion than the Keller–Miksis equation predicts.

A mesh resolution dependence study is shown in figure 17(*b*), using the case of a bubble near a perforated plate with the same geometric parameters as in figure 4(*e–h*). The grid

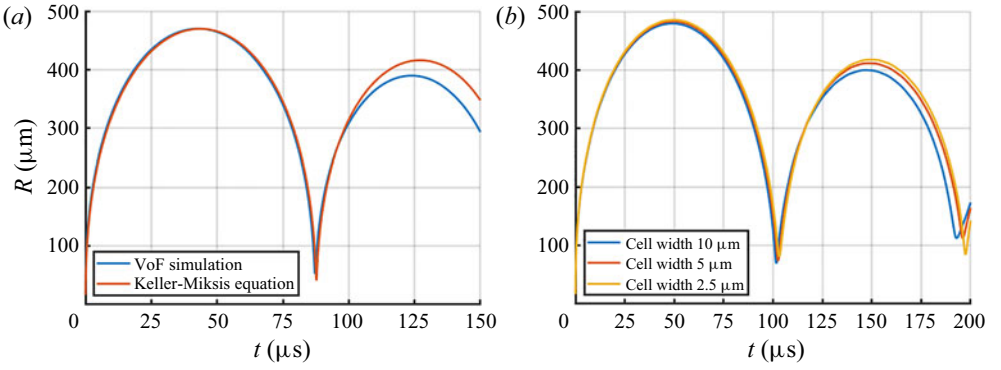

Figure 17. (*a*) Comparison between a VoF simulation of a cavitation bubble far from any boundaries in a large geometry (100 mm × 50 mm) and a solution of the Keller–Miksis equation for a radially oscillating bubble with equal maximum bubble radius R_{max} and (*b*) grid dependence study for the case of a bubble near a perforated boundary for $l = 1000\,\mu\text{m}$, $r_c = 50\,\mu\text{m}$, $d = 500\,\mu\text{m}$.

resolution at the outer boundary of the geometry was kept constant, while the region including the bubble and the channel were discretised using square cells with a width of 10, 5 and 2.5 μm. A cell width of 2.5 μm was used in the rest of this work. For a better direct comparison between different cell sizes, a cylindrical bubble is seeded without interface smearing, and the seed size is kept constant at a radius of 10 μm and a height of 20 μm. For finer meshes, the bubble reaches a slightly larger maximum radius and exhibits a sharper liquid–gas interface. The interface of the thin liquid film that forms between the bubble and the wall after the first collapse is sharper with a finer mesh.

Appendix B. Estimation of the pumped volume

Here we aim to estimate the pumped volume in dependence of the liquid viscosity μ and the channel radius r_c in general form including later times than the simulation covers, i.e. $t > 200\,\mu\text{s}$. We neglect the driving force associated with the bubble dynamics. The laminar volumetric flow rate $\dot{V}$ in a cylindrical channel is given via the Hagen–Poiseuille equation (Pfitzner 1976):

$$\dot{V} = \frac{\pi r_c^4 \Delta p}{8\mu l}. \tag{B1}$$

The pressure drop Δp is in equilibrium with the viscous forces acting upon the fluid in the channel. If the flow driving force taken away, viscosity decelerates the flowing liquid via

$$\Delta p = -\frac{F}{A} = -\frac{\rho A l \dot{u}}{A} = -\frac{\rho l \ddot{V}}{\pi r_c^2}, \tag{B2}$$

turning (B1) into a differential equation for the flow rate $\dot{V}$:

$$\dot{V} = -\frac{r_c^2 \rho}{8\mu}\ddot{V}. \tag{B3}$$

Equation (B3) is solved by

$$\dot{V}(t) = \exp\left(-\frac{8\mu}{r_c^2 \rho} t\right)\dot{V}_0. \tag{B4}$$

Integrating (B4) from $t = 0$ to $t = \infty$ gives the total pumped volume:

$$V = \frac{r_c^2 \rho}{8\mu} \dot{V}_0 = \frac{\pi r_c^4 \rho}{8\mu} u_0. \tag{B5}$$

References

Benjamin, T.B. & Ellis, A.T. 1966 The collapse of cavitation bubbles and the pressure thereby produced against solid boundaries. *Phil. Trans. R. Soc. Lond.* A **260** (1110), 221–240.

Best, J.P. & Kucera, A. 1992 A numerical investigation of non-spherical rebounding bubbles. *J. Fluid Mech.* **245**, 137–154.

Blake, J.R. & Gibson, D.C. 1987 Cavitation bubbles near boundaries. *Annu. Rev. Fluid Mech.* **19**, 99–123.

Cao, K., Liu, Y. & Qu, S. 2017 Quantitative microfluidic delivery based on an optical breakdown-driven micro-pump for the fabrication of fiber functional devices. *Opt. Express* **25** (20), 23690–23698.

Cui, P., Zhang, A.M., Wang, S.P. & Wang, Q.X. 2013 Experimental investigation of bubble dynamics near the bilge with a circular opening. *Appl. Ocean Res.* **41**, 65–75.

Dawoodian, M., Dadvand, A. & Nematollahi, A. 2015 Simulation of bubble dynamics near a plate with an aperture in a vertical cylinder using a combined boundary element-finite difference method. *Engng Anal. Bound. Elem.* **59**, 187–197.

Dijkink, R. & Ohl, C.D. 2008 Laser-induced cavitation based micropump. *Lab Chip* **8**, 1676–1681.

Forster, F.K., Bardell, R.L., Afromowitz, M.A., Sharma, N.R. & Blanchard, A. 1995 Design, fabrication and testing of fixed-valve micro-pumps. In *Proc. ASME Fluids Eng. Div.*, vol. 234, pp. 39–44.

Gonzalez-Avila, S.R., Nguyen, D.M., Arunachalam, S., Domingues, E.M., Mishra, H. & Ohl, C.D. 2020 Mitigating cavitation erosion using biomimetic gas-entrapping microtextured surfaces (GEMS). *Sci. Adv.* **6** (13), eaax6192.

Gonzalez-Avila, S.R., Song, C. & Ohl, C.D. 2015 Fast transient microjets induced by hemispherical cavitation bubbles. *J. Fluid Mech.* **767**, 31–52.

Hickling, R. & Plesset, M.S. 1963 The collapse of a spherical cavity in a compressible liquid. *Office Naval Res. Dep. Navy Div. Engng Appl. Sci.* **24** (85), 1–27.

Kannan, Y.S., Balusamy, S. & Karri, B. 2015 Laser diagnostics for characterization of sprays formed by a collapsing non-equilibrium bubble. In *J. Phys.: Conf. Ser.*, vol. 656, pp. 1–4.

Karri, B., Gonzalez-Avila, S.R., Loke, Y.C., O'Shea, S.J., Klaseboer, E., Khoo, B.C. & Ohl, C.D. 2012*a* High-speed jetting and spray formation from bubble collapse. *Phys. Rev.* E **85** (1), 015303.

Karri, B., Ohl, S.W., Klaseboer, E., Ohl, C.D. & Khoo, B.C. 2012*b* Jets and sprays arising from a spark-induced oscillating bubble near a plate with a hole. *Phys. Rev.* E **86** (3), 036309.

Karri, B., Pillai, K.S., Klaseboer, E., Ohl, S.W. & Khoo, B.C. 2011 Collapsing bubble induced pumping in a viscous fluid. *Sens. Actuators* A **169** (1), 151–163.

Keller, J.B. & Miksis, M. 1980 Bubble oscillations of large amplitude. *J. Acoust. Soc.* **68** (2), 628–633.

Khoo, B.C., Klaseboer, E. & Hung, K.C. 2005 A collapsing bubble-induced micro-pump using the jetting effect. *Sens. Actuators* A **118** (1), 1352–1361.

Koch, M., Lechner, C., Reuter, F., Köhler, K., Mettin, R. & Lauterborn, W. 2016 Numerical modeling of laser generated cavitation bubbles with the finite volume and volume of fluid method, using OpenFOAM. *Comput. Fluids* **126**, 71–90.

Lauterborn, W. & Bolle, H. 1975 Experimental investigations of cavitation-bubble collapse in the neighbourhood of a solid boundary. *J. Fluid Mech.* **72** (2), 391–399.

Lechner, C., Lauterborn, W., Koch, M. & Mettin, R. 2020 Jet formation from bubbles near a solid boundary in a compressible liquid: numerical study of distance dependence. *Phy. Rev. Fluids* **5** (9), 093604.

Lew, K.S.F., Klaseboer, E. & Khoo, B.C. 2007 A collapsing bubble-induced micropump: an experimental study. *Sens. Actuators* A **133** (1), 161–172.

Moloudi, G., Dadvand, A., Dawoodian, M. & Saleki-Haselghoubi, N. 2019 Oscillation of a transient bubble near an aperture made in a convex rigid plate. *Engng Anal. Bound. Elem.* **103**, 51–65.

OpenFOAM 4.0 2016 https://openfoam.org/version/4-0/.

Pfitzner, J. 1976 Poiseuille and his law. *Anaesthesia* **31** (2), 273–275.

Rayleigh, Lord 1917 VIII. On the pressure developed in a liquid during the collapse of a spherical cavity. *Lond. Edinburgh Dublin Phil. Mag. J. Sci.* **34** (200), 94–98.

Reuter, F., Gonzalez-Avila, S.R., Mettin, R. & Ohl, C.D. 2017 Flow fields and vortex dynamics of bubbles collapsing near a solid boundary. *Phys. Rev. Fluids* **2** (6), 064202.

Reuter, F. & Kaiser, S.A. 2019 High-speed film-thickness measurements between a collapsing cavitation bubble and a solid surface with total internal reflection shadowmetry. *Phys. Fluids* **31** (9), 097108.

REUTER, F. & METTIN, R. 2016 Mechanisms of single bubble cleaning. *Ultrason. Sonochem.* **29**, 550–562.
REUTER, F. & OHL, C.D. 2021 Supersonic needle-jet generation with single cavitation bubbles. *Appl. Phys. Lett.* **118** (13), 134103.
SHUTLER, N.D. & MESLER, R.B. 1965 A photographic study of the dynamics and damage capabilities of bubbles collapsing near solid boundaries. *Trans. ASME: J. Fluids Engng* **87** (2), 511–517.
SILBERRAD, D. 1912 Propeller erosion. *Engng* **33**, 33–35.
WANG, S.P., ZHANG, A.M., LIU, Y.L. & WU, C. 2013 Experimental research on bubble dynamics near circular hole of plate. *Wuli Xuebao/Acta Phys. Sin.* **62** (6), 064703.
ZENG, Q., GONZALEZ-AVILA, S.R., DIJKINK, R., KOUKOUVINIS, P., GAVAISES, M. & OHL, C.D. 2018 Wall shear stress from jetting cavitation bubbles. *J. Fluid Mech.* **846**, 341–355.